Macromolecules

pubs.acs.org/Macromolecules Article

Bimodal Rates for Cavitation-Induced Chain Exchange Between Micelles

Taylor Larison, Eric Williams, Coby S. Collins, Sai Venkatesh Pingali, and Morgan Stefik*

Cite This: https://doi.org/10.1021/acs.macromol.3c01040 Read Online

ACCESS | Metrics & More | Article Recommendations | Supporting Information

ABSTRACT: Ultrasonic cavitation temporarily activates chain exchange for otherwise kinetically trapped block polymer micelles. Initial studies of cavitation-induced exchange (CIE) examined dilute polymer concentrations (0.1−1.0 wt %) with low extents of mixing ($R(t)$ of ∼0.9 or ∼10% mixed). This study examines CIE kinetics with *in situ* SANS measurements during continuous ultrasonication for extended timescales that reach deeper extents of mixing ($R(t)$ of ∼0.6 or ∼40% mixed) with semidilute polymer concentrations (1.0−5.0 wt %). All these time-dependent measurements revealed two distinct mixing rates: a fast initial rate for ∼15 min followed by transition to a 10.8x slower steady rate corresponding to the transition from gas-bubbles to vapor-bubbles. The faster rate of chain exchange for gas-bubble cavitation further connects the CIE to surface area turnover as the rate-limiting step. Both regimes had exchange rates that were directly proportional to the polymer concentration without apparent steric hindrances, suggesting that neither gas-bubble nor vapor-bubble cavitation heat was rate-limiting.

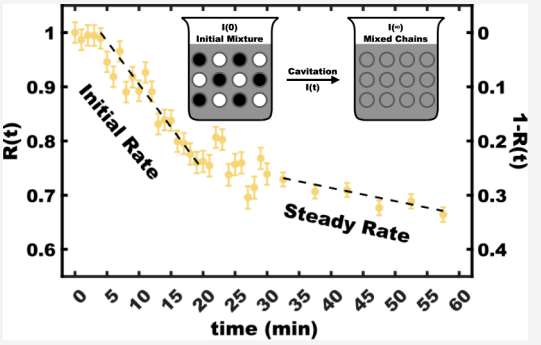

INTRODUCTION

Polymer micelles have found significant uses in applications such as templates for porous materials,[1−7] drug delivery,[8−11] nanoreactors,[12,13] and emulsions.[14] For these applications, the overall aggregation number of micelles (i.e., size) can impact the overall performance of the final application.[15,16] The equilibrium micelle size is a free-energy balance that depends on interfacial enthalpy (χ-dependent), entropy of chain stretching, and other contributions.[17] In contrast to equilibrating conditions, high-χN conditions can lead to persistent (kinetically trapped) micelles by suppressing chain exchange.[18−24] Such persistent micelles have advantages in terms of size stability;[4,25−28] however, size homogenization and equilibration are inherently difficult when chain exchange is suppressed.[29−32]

Cavitation-induced chain exchange (CIE) was recently identified as a way to temporarily introduce chain exchange between otherwise persistent micelles.[18,24] Ultrasonic waves can induce bubble formation in solvents that will grow and then implode (cavitate), sometimes producing ephemeral conditions with high pressures and temperatures greater than 5000 K.[33−35] These cavitation events are often considered adiabatic with the energy being localized to a limited spatial extent of approximately 50 nm.[34] Related rapid and localized heating methods have led to unique block polymer responses in several domains.[36−40] Studies of CIE to date have been limited to dilute polymer concentrations (0.1−1.0 wt %)[18] with low extents of mixing (10% mixed) due to the concomitant size change in that study. There, the initial rate of chain exchange via CIE was directly proportional to the polymer concentration, scaling with the probability of micelle−bubble interactions. However, this concentration dependence is also consistent with other mechanism hypotheses, e.g., direct interaction of micelles with acoustic waves generated from sonication. Furthermore, the rate trends were not examined into deeper mixing regimes or higher polymer concentrations within the semidilute regime.

Chain mixing is often measured using time-resolved small-angle neutron scattering (TR-SANS).[18−24,41−47] Here, the specific rates of micelle chain exchange vary widely, with the methods used to induce mixing. A prior study reported both ∼8.5 and ∼5.5 kg/mol poly(ethylene oxide-*b*-butadiene) dispersed in water that resulted in negligible chain exchange when quiescent over the course of 8 days.[19] However, a similar polymer of equivalent composition with a larger molar mass (∼11.1 kg/mol) was found upon stirring to undergo size changes (evidence of chain exchange) on a week timescale.[21] This same polymer was later found to fully mix under 10 min when vortexed.[20] The proposed agitation-induced chain exchange (AICE) mechanism was associated with surface

Received: May 25, 2023
Revised: August 25, 2023

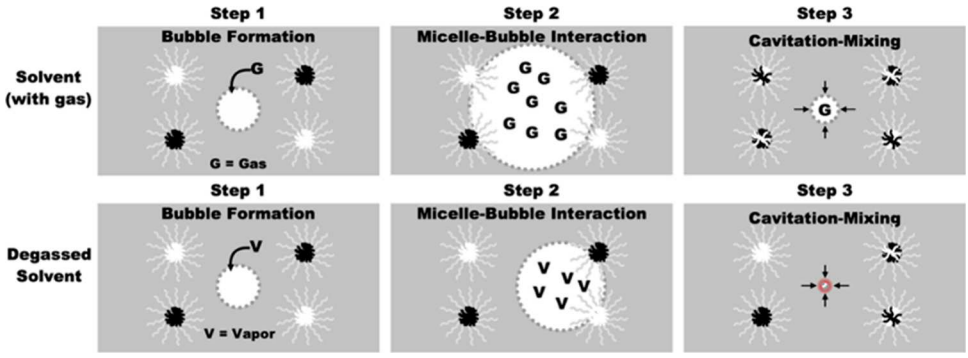

Figure 1. Proposed steps (left-to-right) of cavitation-induced exchange include (1) bubble formation, (2) micelle−bubble interactions (mechanistic details of step 2 are unknown), and (3) cavitation-induced mixing (step 3). Dissolved gases are known to increase the rate of bubble formation and the bubble size (top row). Dissolved gases enter the bubble (gas-bubble), which persists after cavitation and exits the solvent, decreasing the dissolved gas content. In contrast, degassed solvents form vapor-bubbles, which cavitate to a null point (condensation) with higher local energy density (bottom row).

area turnover (surface production and destruction) where micelles undergo chain exchange as a result of micelle−surface interactions.[20] There, the rate of AICE was relatively constant with the polymer concentration until it decreased at higher concentrations ($\geq \sim$1 wt %) as attributed to steric hindrances. Similar to AICE, CIE was speculated to depend upon surface area turnover in part due to the linear time dependence of mixing with sonication time. CIE is unique in that the chain exchange rate accelerated with an increasing polymer concentration, presumably due to the temporary high temperature conditions overcoming the steric barriers of AICE that onset at $\sim$1 wt % polymer concentrations.[18]

The hypothesized micelle−bubble interactions underlying the CIE mechanism can be parsed into distinct steps: (1) bubble surface area formation where the term bubble includes the initial void, solvent vapor, or gas without presuming a specific internal pressure, (2) micelle−bubble interactions where, e.g., chains or micelles may absorb on the bubble interface, and (3) the reduction of the bubble surface area (bubble cavitation), driving chain mixing (Figure 1). A related hypothesis is that the high shear flow from cavitation drives chain mixing in nearby micelles without presuming micelle/chain absorption. Regardless, the dissolved gas content of a solution has significant impacts. Generally, dissolved gases promote gas-bubble formation with faster bubble area production (m^2/s), longer bubble lifetimes (s), and less localized cavitation energy (J/m^3). The increased lifetime results in increased bubble coalescence and a further increase in the surface area change (Figure 1 step 2). Furthermore, the cavitation (collapse) of gas-bubbles can end with a persistent bubble, spreading the heat over a larger zone (Figure 1 step 3). In contrast, cavitation of vapor-bubbles can localize this heat to a point (vapor condensation), which is why degassed solutions are preferred for ultrasonic cleaning applications with more localized energy for agitation (Figure 1 step 3).[48] For CIE, changes to these steps could alter the overall mixing rates. Ultrasonic cavitation is known to result in solution degassing where the timescale varies widely depending on the apparatus.[49,50] Whereas ultrasonication of fresh solutions with dissolved gas tends to form gas-bubbles, the ultrasonication of degassed solutions results in vapor-bubbles (solvent vapor). The rate-limiting step of CIE remains unknown, e.g., dissolved gases should accelerate steps 1 and 2, whereas degassed solutions should accelerate step 3. Observing chain exchange kinetics through solvent degassing can reveal which steps could be rate-limiting. Lastly, a new TR-SANS sample holder was developed to monitor CIE rates *in situ* over long timescales (up to 2 h).

EXPERIMENTAL SECTION

Materials. All materials were used as received, unless specified otherwise. This manuscript uses g/mol units for molar mass as advised by the present IUPAC guide for polymer naming[51] though IUPAC also advises Daltons as an equivalent unitless quantity.[52] Poly(ethylene glycol) methyl ether (PEO−OH, M_n = 5000 g/mol, Aldrich), 2,2-bromopropionic acid (>99%, Aldrich), 4-(dimethylamino)pyridine (DMAP, 99%, Alrdich), *N,N′*-dicyclohexylcarbodiimide (DCC, 99%, BeanTown Chemical), acryloyl chloride (96%, stabilized with 400 ppm phenothiazine, Alfa Aesar), 4-methoxyphenol (99%, Acros Organics), triethylamine (TEA, >99.5%, Millipore Sigma), and dimethylformamide (97%, Aldrich) were used as received. The catalyst, copper(I) bromide (99.99%, Aldrich), ligand, tris[2-(dimethylamino)ethyl]amine (97%, Aldrich), and anhydrous inhibitor-free tetrahydrofuran (THF, 99% Aldrich) were stored inside a glovebox and used as received. Methanol (MeOH, 99.8%, Fisher) was dried at room temperature by storage over 30% w/v molecular sieves (3 Å, 8−12 mesh, Acros Organics) for a week.[53] Deuterium oxide (D_2O, 99.9% D) and deuterated methanol (MeOD, 99.9% D4) were purchased from Cambridge Isotopes and used as received. Methyl acrylate (99%, stabilized) was added to an alumina column prior to use.

Poly(ethylene oxide) Macroinitiator Synthesis. PEO-Br was synthesized via Steglich esterification. Poly(ethylene glycol) monomethyl ether with a molar mass of 5000 g/mol (20 g, 4.0 mmol) was dissolved in 100 mL of methanol-free chloroform. Next, 2-bromopropionic acid (0.720 mL, 8.00 mmol) was added dropwise while stirring. The solution was brought to 0 °C for 10 min prior to the addition of *N,N′*-dicyclohexylcarbodiimide (DCC) (1.65 g, 8.0 mmol) and 4-dimethyl-aminopyridine (DMAP) (0.391 g, 3.20 mmol). The suspension was then allowed to stir for 2 h at 0 °C, brought to room temperature, and allowed to stir overnight. The crude product was isolated via vacuum filtration to remove the urea byproduct. The filtrate was then added to hexane (1000 mL) to isolate the PEO-Br macroinitiator. The precipitate was collected via vacuum filtration and allowed to dry in a vacuum chamber overnight. The final product was collected for an 87% yield as verified with ^{1}H NMR.

Deuterated Methyl Acrylate (DMA) Synthesis. Deuterated methanol (MeOD) (15 mL, 13.32 g, 0.37 mol) and TEA (46 mL, 33.38 g, 0.33 mol) were added to anisole (80 mL) in a round-bottom flask with an addition funnel attached and placed in an ice bath. In the addition funnel, acryloyl chloride (27 mL, 29.86 g, 0.33 mol) and anisole (30 mL) were added. The reaction flask was sparged with nitrogen for 30 min. The acryloyl chloride solution was then added

https://doi.org/10.1021/acs.macromol.3c01040
Macromolecules XXXX, XXX, XXX−XXX

dropwise to the MeOD solution, and the suspension was stirred at room temperature overnight. Then, a water wash was performed with 100 mL of H_2O, and the aqueous layer was removed. The water wash was repeated two more times followed by a wash with 1 M HCl (100 mL), and the organic layer was collected. Excess water was removed with magnesium sulfate, and the suspension was filtered. The final product was collected by distillation of the filtrate at ∼145 to 155 °C. Final product conversion was validated via ^{1}H NMR and ^{13}C NMR (Figures S1 and S2).

Protiated Poly(ethylene oxide-*b*-methyl acrylate) (EO-HMA) Synthesis. EO-HMA was synthesized via atom transfer radical polymerization (ATRP). Previously synthesized PEO-Br (1 g, 0.2 mmol) and methyl acrylate (4.216 g, 49 mmol) were dispersed in 1 mL of anisole. The solution was treated with 3 cycles of freeze−pump−thaw to remove oxygen and was brought into an argon glovebox. A copper stock solution of copper(I) bromide (35.86 mg, 0.25 mmol) and Me6TREN (66.81 mL, 57.6 mg, 0.25 mmol) was dispersed in 0.5 mL of toluene. To the PEO-Br and MA solution, 0.2 mL of copper stock solution was added. The combined solution was then placed in a preheated oil bath at 80 °C and stirred for 16 h. The final product was collected by precipitation in methanol and dried in a vacuum chamber overnight. The final product was validated with ^{1}H NMR and GPC (Figures S3 and S4).

Deuterated Poly(ethylene oxide-*b*-methyl acrylate) (EO-DMA) Synthesis. EO-DMA was also synthesized via ATRP. Previously synthesized PEO-Br (1 g, 0.2 mmol) and previously synthesized DMA (5.342 g, 60 mmol) were dispersed in 1 mL of anisole. The solution was treated with 3 cycles of freeze−pump−thaw to remove oxygen and brought into an argon glovebox. To the PEO-Br and MA solution, 0.2 mL of the described copper stock solution was added. The solution was then placed in a preheated oil bath at 80 °C and stirred for 22 h. The final product was collected by precipitation in methanol and dried in a vacuum chamber overnight. The final product was validated with ^{1}H NMR and GPC (Figures S4 and S5).

SANS Sample Preparation. A total of 3 samples were measured for each respective concentration: $I(\infty)$, $I(0)$, and $I(t)$. A premixed sample, $I(\infty)$, was generated by mixing equal moles of EO-HMA and EO-DMA in a good solvent before removal of the solvent and micellization, as described below. The time-dependent sonicated sample, $I(t)$, was prepared by separately micellizing EO-HMA and EO-DMA polymers, as described below, followed by their combination in an equal molar ratio. The unmixed sample, $I(0)$, corresponded to $I(t)$ at $t = 0$, i.e., prior to any ultrasonication. Micelle solutions were prepared by dispersing the indicated polymers in methanol at a concentration of 10 wt % followed by the addition of a H_2O/D_2O (77.16/22.84 vol %) mixture until the final combined solution was 50/50 (vol %) MeOH/(H_2O/D_2O). The polymer was then diluted with a solution of 50/50 (vol %) MeOH/(H_2O/D_2O) until the desired concentration was achieved.

SANS Measurements. SANS measurements were performed on the CG-3 Bio-SANS instrument at the High Flux Isotope Reactor at Oak Ridge National Laboratory.[54,55] A sealed titanium cell with a 2 mm spacer was used for SANS measurements, containing a total of 0.35 mL of the micelle solution. A metal adapter was fabricated to connect the titanium cell to the threaded hole of a piezoelectric transducer (Figure 3a,b). A generic ultrasonic transducer with an included power board was used (YaeCCC 60 W, 40 kHz). Please note that the ultrasonic power delivered to the sample cell is sensitive to the torque of the cell−transducer connection, which can also change as a result of ultrasonication. A hand-tight torque was found to be generally stable and was used for all experiments here. A CPU heat sink and fan were epoxied to one end of the transducer to prevent overheating. This apparatus was placed in a temperature-controlled sample holder held at 25 °C (Figure 3c). An output of the acquisition computer switched the power on/off to the ultrasonic transducer using a 5 V relay (DROK solid-state relay for Arduino based on Omron G3MB-202P). The sample-to-detector distance (7 m) and beam collimation (14 mm) were selected to balance the desire for high flux and improved time resolution against the desire to include a sufficient low-q Guinier region. The SANS acquisition for $I(t)$ was synchronized with the onset of ultrasonication, and the time coordinate feature for every detected neutron of the SANS data facilitated subsequent time interval slicing with flexibility.

Raw SANS data were processed using facility-wide developed DRTSANS reduction software[56] accessed via a Jupyter Notebook script. The inclusion of a time coordinate associated with each detected neutron enabled flexible subsequent time binning. The time value of each reported time slice corresponds to the center of the detected time window, e.g., neutrons detected from minute 5 to minute 10 would be reported as the window centered at 7.5 min. The time window sizes were chosen based on signal-to-noise considerations. Generally, 60 s time slices were used for the first 30 min of $R(t)$ analysis, and 300 s time slices were used for some of the longer sonication times when needed to reduce the uncertainty. The reduced SANS curves used for $R(t)$ analysis were then analyzed to determine the incoherent background scattering intensity using Porod analysis (Figure S6). This involved performing a straight line fit to data on a Porod plot $I(q)\cdot q^4$ vs q^4 and assigning the slope of the straight line as the incoherent background scattering intensity. This background intensity for each reduced SANS curve was determined and subtracted. The area under the resulting background-subtracted curves was calculated by integration from $q = 0.07-8$ nm^{-1}, with the resulting values being plugged into eq 1.

$$R(t) = \sqrt{\frac{I(t) - I(\infty)}{I(0) - I(\infty)}} \tag{1}$$

Error Analysis. Intensity uncertainty was propagated through all calculations. Linear best fit parameters and their error were calculated using a Monte Carlo method similar to the open source linfitxy() program.[57] In brief, normal distributions were assumed for each fitted point based on the propagated uncertainty. A total of 500 distinct data sets were derived using normally distributed random variation, and the corresponding 500 best fits were used to calculate the mean and standard deviation of each fit term.

SANS Fitting. SANS patterns for EO-MA and EO-DMA micelles were fitted using SASfit.[58] There, the "BlockCopolymerMicelle" model was utilized, which was derived by Pedersen and Gertenberg[59,60] and was subsequently reparametrized to include the aggregation number.[58] This model includes terms for the volume of a single core block unit, the volume of a single corona block unit, the amount of solvent in the core, the scattering length density (SLD) of the core, the SLD of the corona, the SLD of the solvent, the aggregation number, the corona radius of gyration, and the extent of corona block penetration into the core. Additionally, a constant background term was included in the fit.

RESULTS AND DISCUSSION

Chain mixing was examined during CIE using TR-SANS measurements under contrast-matched conditions (Figure 2). Protiated poly((ethylene oxide)-*b*-methyl acrylate) (EO-MA)

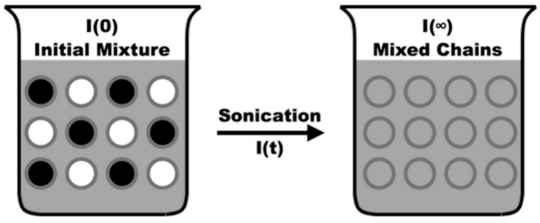

Figure 2. Chain mixing was monitored as a function of scattering intensity where the initial mixture ($I(0)$) of D-(black) and H-(white) labeled micelles had the highest scattering intensity as compared to the contrast-matched solvent (gray). Chain mixing results in decreased scattering intensity until a minimum is reached with fully mixed chains ($I(\infty)$).

https://doi.org/10.1021/acs.macromol.3c01040
Macromolecules XXXX, XXX, XXX−XXX

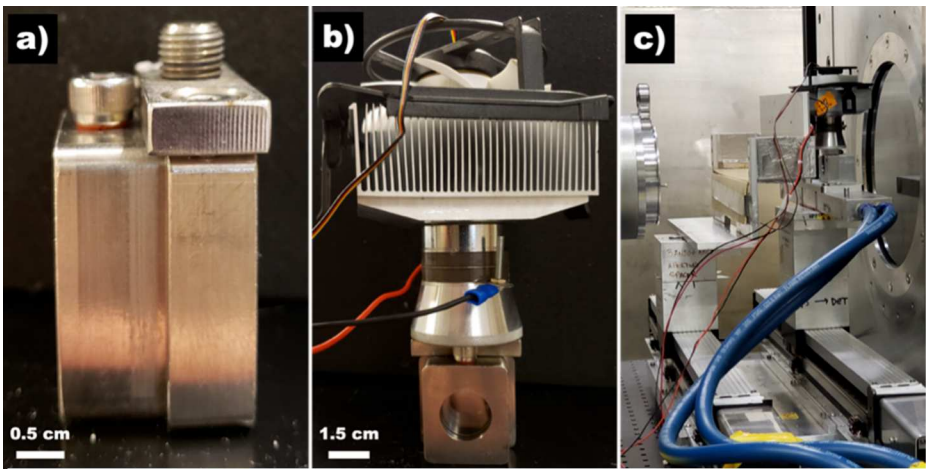

Figure 3. Photographs of the *in situ* ultrasonication setup including (a) the titanium sample cell with a threaded adapter, (b) the mounted ultrasonic transducer assembly with a heat sink and a cooling fan, and (c) the whole ultrasonic assembly placed in a temperature-controlled cell holder on the Bio-SANS instrument.

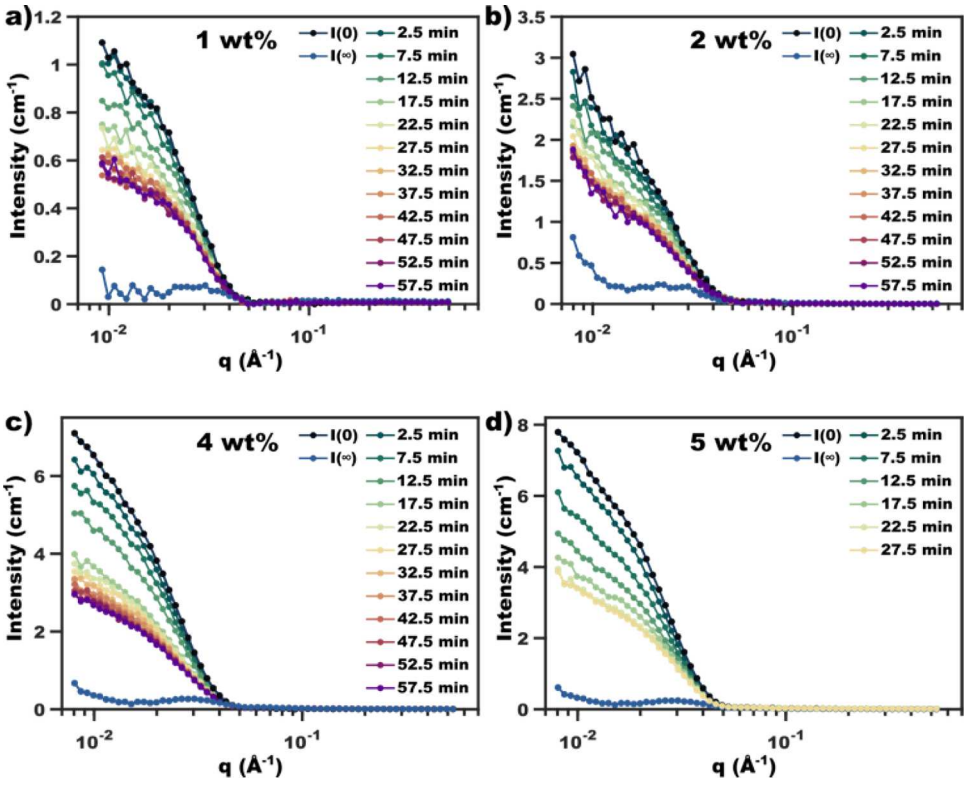

Figure 4. Linear-log SANS curves are presented for experiments performed with (a) 1, (b) 2, (c) 4, and (d) 5 wt % polymer solutions. For each concentration, the initial unmixed condition ($I(0)$), the premixed condition ($I(\infty)$), and the time-dependent conditions $I(t)$ with t = 5−60 min were measured.

and deuterated poly((ethylene oxide)-*b*-methyl acrylate) (EO-DMA) polymers were synthesized from the same 5 kg/mol PEO macroinitiator and had MA/DMA degrees of polymerization of 172 and 178, respectively, with molar mass dispersity less than 1.15 (Table S1 and Figures S1−S5). GPC analysis determined that ∼4 wt % PEO macroinitiator was present in these polymers, which was included when calculating the molar mass dispersity. The reported nominal polymer concentrations spanned a wide range and did not consider this minor systematic error. A MeOH/water mixture was chosen to enable facile micelle dispersion in MeOH followed by kinetic entrapment upon addition of water (higher χ). This strategy enabled quick adjustments to the target solvent composition while at the beamline. The scattering length density (SLD) of the solution was matched to the mixed micelle core equilibrium state, i.e., each micelle core containing equal moles of deuterated and protiated polymers. The contrast match was optimized by adjusting the H_2O/D_2O ratio until the scattering intensity of deuterated micelles was equal to that of the protiated micelles. Thus, the scattered intensity was maximum for the unmixed micelles and progressively decreased with chain mixing (Figure 2). Unless otherwise

https://doi.org/10.1021/acs.macromol.3c01040
Macromolecules XXXX, XXX, XXX−XXX

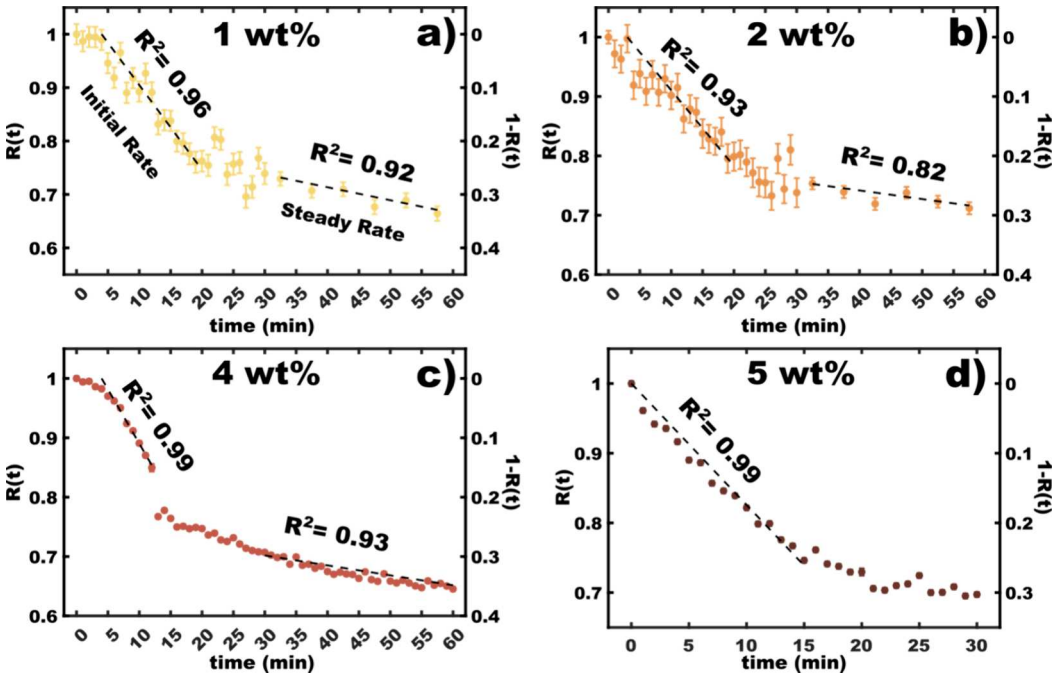

Figure 5. A relaxation function $R(t)$ was calculated for each polymer solution concentration over time, including (a) 1, (b) 2, (c) 4, and (d) 5 wt % polymer. The interpreted extent of mixing $(1 - R(t))$ is plotted as the second y-axis (dashed line). Pearson's correlation coefficient R^2 was calculated for each fitted regime. The error bars correspond to the propagated intensity error. Please note that the fitting of the 4 wt % sample used a shortened initial rate regime to avoid data points affected by an unplanned electronic interruption at t = 13−14 min. The measurement of the 5 wt % was limited to 30 min due to fuel change at the neutron source.

noted, all presented SANS data had sample holder and incoherent background subtracted and were then normalized to sample transmission and thickness to yield absolute scattering units, cm^{-1} (Figure S6). The micelles were also confirmed to be persistent (kinetically trapped) without observable intensity changes due to chain mixing when quiescent (without sonication) for 6 h (Figure S8).

The time-dependent chain mixing during CIE was examined with 4 different polymer concentrations (1, 2, 4, and 5 wt %) from the dilute to the semidilute regime. The transition from the dilute to semidilute regimes was estimated by the appearance of the structure factor between 2 and 4 wt % polymer in EO-MA and EO-DMA SANS curves (Figure S9). An *in situ* sonication setup (Figure 3) was combined with flexibility in time binning during the data reduction of the scattered signal. This feature was afforded by inclusion of a time coordinate associated with each detected neutron. The initial scattering curves generally exhibited a rapid decrease in the overall intensity during the first ∼15−20 min followed by a gradual decrease in the overall intensity corresponding to slower mixing with longer timescales (Figure 4). A relaxation function ($R(t)$, eq 1) was used to quantify the scattered intensity decay as a function of time (Figure 5). The $R(t)$ approach is suitable for measuring chain mixing when the micelle size and morphology are constant. The constant size and morphology of EO-MA and EO-DMA micelles were validated with separate SANS measurements, which confirmed that there were no statistically significant changes to the scattering profiles as a result of ultrasonication (Figure S10). Comparison here of the quiescent and *in situ* ultrasonication SANS data also confirms that there is no detectable intensity change as a result of bubbles (Figure S10). It is noted that a recently developed shifting reference relaxation function (SRR(t)) approach extends the simplicity of $R(t)$ with added tolerance to size and morphology changes.[61] Separate measurements of EO-MA and EO-DMA micelles were most consistent with spherical micelles having a radius of ∼8.6 nm (Figure S7). Here, the analysis of SANS data with $R(t)$ plots clearly shows distinct slopes, indicating that the initial rates are higher than the steady rates. A few minutes induction time was noted for some runs, which was excluded from rate analysis since it was attributed to ultrasonication-induced tightening of the fasteners. Thus, the initial rate regimes were fitted as starting when $R(t) < 0.98$ and then progressing for 15 min from that point. Correspondingly, the steady rate regime was fitted starting 30 min later as informed by the gradual change in slope of $R(t)$ between ∼15 and 30 min. Here, 5 min time slices were used for low polymer concentrations (1−2 wt %) to account for the increased error of the scattered intensity and slow mixing rates in the steady rate regime. These initial rate and steady rate regimes were well-fitted with linear regressions, having Pearson's correlation coefficients of $R^2 > 0.93$ (initial rate) and $R^2 > 0.82$ (steady rate). Here, $1 - R(t)$ corresponds to the mixed chain concentration over time (Figure 5). The sample with a 4 wt % polymer underwent additional ultrasonic time for 80 total min to check for further rate changes; however, the steady rate remained constant within the error of the best fit (Figure S11). Please note that the 4 wt % sample had a pause of sonication at t = 10−11 min due to an electrical fault (Figure 5), which limited the initial rate fitting window. Similarly, the SANS measurement of the 5 wt % sample was ended after 30 min due to fuel change of the neutron source; thus, only the corresponding initial rate was evaluated.

The rates of chain exchange were determined from these data sets. The concentration of mixed chains was calculated at each time point as $C_0 \cdot [1 - R(t)]$ where C_0 is the polymer concentration. Thus, the decay in $R(t)$ is connected to the concentration of mixed chains. The resulting time-dependent

https://doi.org/10.1021/acs.macromol.3c01040
Macromolecules XXXX, XXX, XXX−XXX

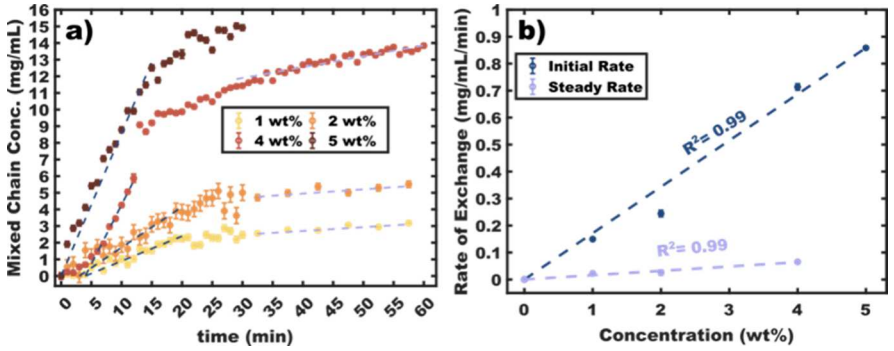

Figure 6. (a) The mixed chain concentration was calculated as $C_0 \cdot [1 - R(t)]$ for each time-dependent concentration series. The error bars correspond to the propagated intensity error. The corresponding initial rate and steady rate regimes (dashed lines) had the indicated Pearson's correlation coefficient R^2 values (Figure 5b). The rate of chain exchange was calculated as the slope of the mixed chain concentration for both the initial rate and steady rate regimes. The error bars correspond to the standard deviation of the best fit slopes.

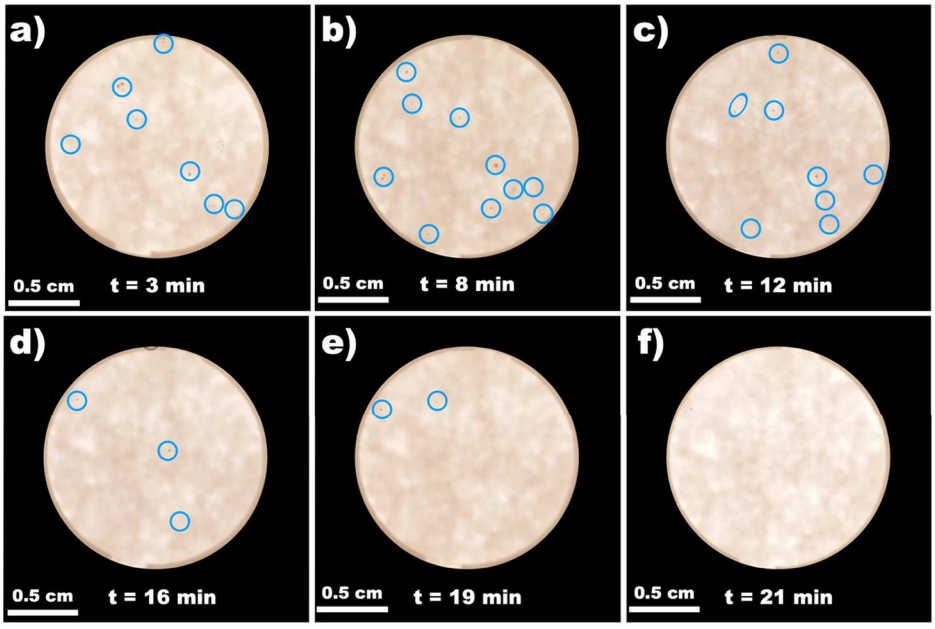

Figure 7. Photographs of the cell window during ultrasonication (MeOH/H_2O/D_2O = 50/38.58/11.42 vol %). Many large bubbles are visible during the first ∼15 min (a−c) followed by relatively few observable bubbles with longer ultrasonication times (d−f). The cell was back illuminated through a sheet of white paper, and visible bubbles were circled for clarity.

plots reveal the initial and steady rates of change to the mixed chain concentration (Figure 6a). The corresponding slopes of these lines are the rates of chain exchange for each time regime (mg/mL/min) (Figure 6b). Similar to the prior CIE study spanning dilute concentrations, the initial rate and steady rate calculated here were directly proportional to the polymer concentrations (R^2 > 0.98). The corresponding best fits indicated that the initial rate of chain exchange (mg/mL/min) = 0.172 ± 0.001 (mg/mL/min/wt %) × polymer concentration (wt %). Correspondingly, the steady rate of exchange (mg/mL/min) = 0.016 ± 0.001 (mg/mL/min/wt %) × polymer concentration (wt %). The slopes of the initial rate and steady rate best fit equations (Figure 5b) indicate that there is an ∼10.8× reduction in the rate of chain exchange when the system transitions from the initial rate to steady rate.

The ∼15−30 min time window to transition out of the initial rate and to the steady rate coincides with the typical time needed for ultrasonic solvent degassing, suggesting that the change in the rate is associated with the dissolved gas content as discussed further in the next paragraph. This time window was examined photographically where early time periods (t < ∼15 min) exhibited many large bubbles, which undulated and moved quickly (Figure 7a−c and Figure S13), consistent with gas-bubbles. Longer time periods (t > ∼15 min) exhibited few visible bubbles, consistent with a transition toward a majority of smaller vapor-bubbles (Figure 7d−f). Thus, the CIE rates of chain exchange correlated with the type of bubble produced by ultrasonication.

The two observed rates of CIE over time elucidate mechanistic features. First though, it is worth noting the experimental aspects that are not likely contributing to the changes in observed rates. A changing temperature of the sample cell is not a suitable explanation since the cell was thermally controlled (Figure 3c), and furthermore, any minor heating would be anticipated to accelerate thermally activated processes rather than the observed deceleration of the CIE rate over time. A changing transducer temperature is also not a likely explanation since the transducer reaches a steady state temperature within the first minute owing to its heat sink with active cooling (Figure 3b). In addition, the extended 80 min

https://doi.org/10.1021/acs.macromol.3c01040
Macromolecules XXXX, XXX, XXX−XXX

measurement of CIE for the 4 wt % sample did not exhibit further changes to the steady rate, also supporting constant transducer output (Figure S9). The direct interaction of acoustic waves with micelles is not a suitable explanation since the ultrasonic power was kept constant throughout the experiment despite the changes in the chain exchange rate. The distribution of chain entanglements is an unlikely explanation for the rate change near 25−30% of mixing since the ∼8.8 kg/mol entanglement molar mass for PMA[62] leads to the expectation of 10−13% of chains being unentangled (Figure S12). Also, the degradation of polymer chains from ultrasonication can be eliminated as an explanation since GPC measurements after ultrasonication were consistent with the parent polymers (Figure S4), similar to earlier CIE studies.[1] As discussed in the Introduction, dissolved gases could accelerate CIE steps 1 and 2, whereas the degassed solvent could accelerate CIE step 3 (Figure 1). Since the initial rate was larger than the steady rate, these data suggest that either step 1 or 2 is rate-limiting for CIE. The increasing rate of CIE with the polymer concentration here is remarkable considering that the rate of AICE was slowed once polymer concentrations exceeded ∼1 wt %. Similarly, SCE was found to be nearly independent of the polymer concentration for low concentrations (0.5−2.0 vol %) and then decelerated significantly at higher concentrations (15 vol %).[63] In contrast, these data show that the rate of CIE is directly proportional to the polymer concentration well into the semidilute regime (up to 5 wt %) without any apparent steric hindrances. This concentration dependence is presumably associated with the localized heat of the cavitation events providing sufficient activation energy to overcome such barriers, both from the cavitation of gas-bubbles and cavitation of vapor-bubbles. It is noteworthy that the cavitation heat is expected to be higher for degassed solvents (steady rate); however, on the contrary, the fastest chain exchange was found with dissolved gases (initial rate). The concentration-dependent and dissolved-gas-dependent CIE rates thus suggest that cavitation heat is not rate-limiting (step 3). This is the first study to compare vapor-bubbles to gas-bubbles produced by the CIE and thus provides the strongest mechanistic evidence for the CIE to date. Potential future studies include the possibility to reach the steady rate at $t = 0$ with a degassed solvent, the ability to maintain the initial rate with continuous gas sparging, and studying the effects of sonication frequency and sonication power.[64−67] Similarly, molecular parameters such as the effects of core/solvent (χ) selection and molar mass (N) remain unknown and are open for future studies. If the cavitation heat is in large excess of the activation energy, then there may not be an effect of χN until polymer entanglement hinders chain exchange. The new data presented here further emphasize the central role of bubble interfaces enabling CIE where either step 1 or step 2 is rate-limiting (Figure 1).

CONCLUSIONS

An *in situ* ultrasonication apparatus was developed to observe the CIE over extended periods. Contrast-matched experiments revealed chain mixing as a decrease in the scattered intensity, which enabled calculation of the mixed chain concentration and the chain mixing rate. The chain mixing rate was found to be bimodal with an ∼10.8x rate decrease over time. The change from the CIE initial rate to the steady rate correlated with the observed time for solvent degassing and thus the known transition from gas-bubbles to vapor-bubbles. Whereas dissolved gases promote larger and longer-lived bubbles, the cavitation of degassed solvents is known to be more energetic locally. Thus, the faster initial CIE rate suggests a central rate-limiting role for bubble interfaces. Furthermore, the directly proportional CIE rate (both the initial rate and the steady rate) to the polymer concentration suggests that CIE is not limited by concentration-dependent energetic barriers as noted for other chain exchange mechanisms. Lastly, the acceleration of CIE with the polymer concentration was shown to extend into the semidilute regime (5 wt %), which is unique among other chain exchange mechanisms.

ASSOCIATED CONTENT

Supporting Information

The Supporting Information is available free of charge at https://pubs.acs.org/doi/10.1021/acs.macromol.3c01040.

NMR experiments, GPC traces, polymer tables, Porod background corrections, fit parameters, SANS fits, quiescent data, EO-MA and EO-DMA SANS curves, SANS curves during ultrasonication without mixing, 4 wt % extended sonication time $R(t)$ values, polymer entanglement distributions, and photos of ultrasonication (PDF)

AUTHOR INFORMATION

Corresponding Author

Morgan Stefik − *Department of Chemistry and Biochemistry, University of South Carolina, Columbia, South Carolina 29208, United States;* orcid.org/0000-0002-2645-7442; Email: morgan@stefikgroup.com

Authors

Taylor Larison − *Department of Chemistry and Biochemistry, University of South Carolina, Columbia, South Carolina 29208, United States;* orcid.org/0000-0002-4418-9330

Eric Williams − *Department of Chemistry and Biochemistry, University of South Carolina, Columbia, South Carolina 29208, United States*

Coby S. Collins − *Department of Chemistry and Biochemistry, University of South Carolina, Columbia, South Carolina 29208, United States*

Sai Venkatesh Pingali − *Neutron Scattering Division, Oak Ridge National Laboratory, Oak Ridge, Tennessee 37831, United States;* orcid.org/0000-0001-7961-4176

Complete contact information is available at: https://pubs.acs.org/10.1021/acs.macromol.3c01040

Notes

The authors declare no competing financial interest.

ACKNOWLEDGMENTS

T.L., E.W., C.C., and M.S. acknowledge support by the National Science Foundation under NSF Award No. DMR-1752615. We thank the University of Minnesota Chemical Engineering and Materials Science department for GPC data. This work made use of the resources at the High Flux Isotope Reactor, a DOE Office of Science User Facility operated by the Oak Ridge National Laboratory (IPTS-21752.1 and IPTS 25337.1). The research at Oak Ridge National Laboratory's Center for Structural Molecular Biology (CSMB), which operates the Bio-SANS instrument, was supported by the U.S. Department of Energy, Office of Science, through the Office of

Biological and Environmental Research under Contract FWP ERKP291, using facilities supported by the Office of Basic Energy Research, U.S. Department of Energy. This manuscript has been authored by UT-Battelle, LLC, under Contract No. DE-AC05-00OR22725 with the U.S. Department of Energy. The United States Government retains and the publisher, by accepting the article for publication, acknowledges that the United States Government retains a nonexclusive, paid-up, irrevocable, worldwide license to publish or reproduce the published form of this manuscript, or allow others to do so, for United States Government purposes. The Department of Energy will provide public access to these results of federally sponsored research in accordance with the DOE Public Access Plan (http://energy.gov/downloads/doe-public-access-plan). We thank Dr. Ting Ge for helpful discussions.

REFERENCES

(1) Lee, J.; Christopher Orilall, M.; Warren, S. C.; Kamperman, M.; Disalvo, F. J.; Wiesner, U. Direct Access to Thermally Stable and Highly Crystalline Mesoporous Transition-Metal Oxides with Uniform Pores. *Nat. Mater.* **2008**, *7* (3), 222−228.

(2) Zhao, D.; Feng, J.; Huo, Q.; Melosh, N.; Fredrickson, G. H.; Chmelka, B. F.; Stucky, G. D. Triblock Copolymer Syntheses of Mesoporous Silica with Periodic 50 to 300 Angstrom Pores. *Science* **1998**, *279* (5350), 548−552.

(3) Van Den Bergh, W.; Williams, E. R.; Vest, N. A.; Chiang, P. H.; Stefik, M. Mesoporous TiO2Microparticles with Tailored Surfaces, Pores, Walls, and Particle Dimensions Using Persistent Micelle Templates. *Langmuir* **2021**, *37* (44), 12874−12886.

(4) Williams, E. R.; McMahon, P. L.; Reynolds, J. E.; Snider, J. L.; Stavila, V.; Allendorf, M. D.; Stefik, M. Tailored Porous Carbons Enabled by Persistent Micelles with Glassy Cores. *Mater. Adv.* **2021**, *2* (16), 5381−5395.

(5) Lantz, K. A.; Clamp, N. B.; van den Bergh, W.; Sarkar, A.; Stefik, M. Full Gamut Wall Tunability from Persistent Micelle Templates via Ex Situ Hydrolysis. *Small* **2019**, *15* (18), 1−10, DOI: 10.1002/smll.201900393.

(6) Lokupitiya, H. N.; Jones, A.; Reid, B.; Guldin, S.; Stefik, M. Ordered Mesoporous to Macroporous Oxides with Tunable Isomorphic Architectures: Solution Criteria for Persistent Micelle Templates. *Chem. Mater.* **2016**, *28* (6), 1653−1667.

(7) Stefik, M.; Guldin, S.; Vignolini, S.; Wiesner, U.; Steiner, U. Block Copolymer Self-Assembly for Nanophotonics. *Chem. Soc. Rev.* **2015**, *44* (15), 5076−5091.

(8) Lee, E. S.; Gao, Z.; Kim, D.; Park, K.; Kwon, I. C.; Bae, Y. H. Super PH-Sensitive Multifunctional Polymeric Micelle for Tumor PHe Specific TAT Exposure and Multidrug Resistance. *J. Controlled Release* **2008**, *129* (3), 228−236.

(9) Kataoka, K.; Harada, A.; Nagasaki, Y. Block Copolymer Micelles for Drug Delivery: Design, Characterization and Biological Significance. *Adv. Drug Delivery Rev.* **2012**, *64* (SUPPL.), 37−48, DOI: 10.1016/j.addr.2012.09.013.

(10) Chopra, P.; Hao, J.; Li, S. K. Sustained Release Micellar Carrier Systems for Iontophoretic Transport of Dexamethasone across Human Sclera. *J. Controlled Release* **2012**, *160* (1), 96−104.

(11) Mura, S.; Nicolas, J.; Couvreur, P. Stimuli-Responsive Nanocarriers for Drug Delivery. *Nat. Mater.* **2013**, *12* (11), 991−1003.

(12) Liu, Y.; Wang, Y.; Wang, Y.; Lu, J.; Piñón, V.; Weck, M. Shell Cross-Linked Micelle-Based Nanoreactors for the Substrate-Selective Hydrolytic Kinetic Resolution of Epoxides. *J. Am. Chem. Soc.* **2011**, *133* (36), 14260−14263.

(13) Kaur, R.; Khullar, P. Block Copolymer Micelles as Nanoreactors for the Synthesis of Gold Nanoparticles. *Mater. Biomed. Eng.: Inorg. Micro- Nanostruct.* **2019**, 177−210.

(14) Alexandridis, P.; Hatton, T. Poly(Ethylene Oxide)Poly(Propylene Oxide)Poly(Ethylene Oxide) Block Copolymer Surfactants in Aqueous Solutions and at Interfaces: Thermodynamics, Structure, Dynamics, and Modeling. *Colloids Surf., A* **1995**, *96* (1−2), 1−46, DOI: 10.1016/0927-7757(94)03028-X.

(15) Anraku, Y.; Kishimura, A.; Kobayashi, A.; Oba, M.; Kataoka, K. Size-Controlled Long-Circulating PICsome as a Ruler to Measure Critical Cut-off Disposition Size into Normal and Tumor Tissues. *Chem. Commun.* **2011**, *47* (21), 6054−6056.

(16) Nel, A. E.; Mädler, L.; Velegol, D.; Xia, T.; Hoek, E. M. V.; Somasundaran, P.; Klaessig, F.; Castranova, V.; Thompson, M. Understanding Biophysicochemical Interactions at the Nano-Bio Interface. *Nat. Mater.* **2009**, *8* (7), 543−557.

(17) Linse, P. *Amphiphilic Block Copolymers Self-Assembly and Applications*; Alexandridis, P.; Lindman, B., Eds.; Elsevier, 2000.

(18) Lantz, K. A.; Sarkar, A.; Littrell, K. C.; Li, T.; Hong, K.; Stefik, M. Cavitation Enables Switchable and Rapid Block Polymer Exchange under High- χ N Conditions. *Macromolecules* **2018**, *51* (17), 6967−6975.

(19) Won, Y. Y.; Davis, H. T.; Bates, F. S. Molecular Exchange in PEO-PB Micelles in Water. *Macromolecules* **2003**, *36* (3), 953−955.

(20) Murphy, R. P.; Kelley, E. G.; Rogers, S. A.; Sullivan, M. O.; Epps, T. H. Unlocking Chain Exchange in Highly Amphiphilic Block Polymer Micellar Systems: Influence of Agitation. *ACS Macro Lett.* **2014**, *3* (11), 1106−1111.

(21) Kelley, E. G.; Murphy, R. P.; Seppala, J. E.; Smart, T. P.; Hann, S. D.; Sullivan, M. O.; Epps, T. H. Size Evolution of Highly Amphiphilic Macromolecuar Solution Assemblies via a Distince Bimodal Pathway. *Nat. Commun.* **2014**, *5*, 3599.

(22) Choi, S. H.; Lodge, T. P.; Bates, F. S. Mechanism of Molecular Exchange in Diblock Copolymer Micelles: Hypersensitivity to Core Chain Length. *Phys. Rev. Lett.* **2010**, *104* (4), 1−4, DOI: 10.1103/PhysRevLett.104.047802.

(23) Lu, J.; Choi, S.; Bates, F. S.; Lodge, T. P. Molecular Exchange in Diblock Copolymer Micelles: Bimodal Distribution in Core-Block Molecular Weights. *ACS Macro Lett.* **2012**, *1* (8), 982−985.

(24) Lokupitiya, H. N.; Stefik, M. Cavitation-Enabled Rapid and Tunable Evolution of High-: Xn Micelles as Templates for Ordered Mesoporous Oxides. *Nanoscale* **2017**, *9* (4), 1393−1397.

(25) Stefik, M. Single-Variable Porous Nanomaterial Series from Polymer Structure-Directing Agents. *J. Mater. Res.* **2022**, *37* (1), 25−42.

(26) Larison, T.; Stefik, M. Persistent Micelle Corona Chemistry Enables Constant Micelle Core Size with Independent Control of Functionality and Polyelectrolyte Response. *Langmuir* **2021**, *37* (32), 9817−9825.

(27) van den Bergh, W.; Larison, T.; Jesus Jara Fornerod, M.; Guldin, S.; Stefik, M. Faster Intercalation Pseudocapacitance Enabled by Adjustable Amorphous Titania Where Tunable Isomorphic Architectures Reveal Accelerated Lithium Diffusivity. *Batteries Supercaps* **2022**, *5* (7), No. e202200122, DOI: 10.1002/batt.202200122.

(28) Sarkar, A.; Stefik, M. How to Make Persistent Micelle Templates in 24 h and Know It Using X-Ray Scattering. *J. Mater. Chem. A* **2017**, *5* (23), 11840−11853.

(29) Cameron, N. S.; Corbierre, M. K.; Eisenberg, A. 1998 E.W.R. Steacie Award Lecture Asymmetric Amphiphilic Block Copolymers in Solution: A Morphological Wonderland. *Can. J. Chem.* **1999**, *77* (8), 1311−1326, DOI: 10.1139/v99-141.

(30) Riess, G. Micellization of Block Copolymers. *Prog. Polym. Sci.* **2003**, *28* (7), 1107−1170.

(31) SantosMiranda, M. E.; Marcolla, C.; Rodriguez, C. A.; Wilhelm, H. M.; Sierakowski, M. R.; BelleBresolin, T. M.; Alves de Freitas, R. I. The Role of N-Carboxymethylation of Chitosan in the Thermal Stability and Dynamic. *Polym. Int.* **2006**, *55* (June), 961−969, DOI: 10.1002/pi.

(32) Hayward, R. C.; Pochan, D. J. Tailored Assemblies of Block Copolymers in Solution: It Is All about the Process. *Macromolecules* **2010**, *43* (8), 3577−3584.

(33) Flint, E. B.; Suslick, K. S. The Temperature of Cavitation. *Science* **1991**, *253* (5026), 1397−1399.

https://doi.org/10.1021/acs.macromol.3c01040
Macromolecules XXXX, XXX, XXX−XXX

(34) Cravotto, G.; Cintas, P. Power Ultrasound in Organic Synthesis: Moving Cavitational Chemistry from Academia to Innovative and Large-Scale Applications. *Chem. Soc. Rev.* **2006**, *35* (2), 180−196.
(35) Suslick, K. S.; Flannigan, D. J. Inside a Collapsing Bubble: Sonoluminescence and the Conditions during Cavitation. *Annu. Rev. Phys. Chem.* **2008**, *59*, 659−683.
(36) Zhang, Y.; Bhaway, S. M.; Wang, Y.; Cavicchi, K. A.; Becker, M. L.; Vogt, B. D. Rapid (<3 min) Microwave Synthesis of Block Copolymer Templated Ordered Mesoporous Metal Oxide and Carbonate Films Using Nitrate-Citric Acid Systems. *Chem. Commun.* **2015**, *51* (24), 4997−5000.
(37) Jiang, J.; Jacobs, A. G.; Wenning, B.; Liedel, C.; Thompson, M. O.; Ober, C. K. Ultrafast Self-Assembly of Sub-10 Nm Block Copolymer Nanostructures by Solvent-Free High-Temperature Laser Annealing. *ACS Appl. Mater. Interfaces* **2017**, *9* (37), 31317−31324.
(38) Tan, K. W.; Wiesner, U. Block Copolymer Self-Assembly Directed Hierarchically Structured Materials from Nonequilibrium Transient Laser Heating. *Macromolecules* **2019**, *52* (2), 395−409.
(39) Yu, F.; Zhang, Q.; Thedford, R. P.; Singer, A.; Smilgies, D. M.; Thompson, M. O.; Wiesner, U. B. Block Copolymer Self-Assembly-Directed and Transient Laser Heating-Enabled Nanostructures toward Phononic and Photonic Quantum Materials. *ACS Nano* **2020**, *14* (9), 11273−11282.
(40) Tu, W. H.; Seah, G. L.; Li, Y.; Wang, X.; Tan, K. W. Transient Laser-Annealing-Induced Mesophase Transitions of Block Copolymer−Resol Thin Films. *ACS Polym. Au* **2022**, *2* (1), 42−49.
(41) Lund, R.; Willner, L.; Pipich, V.; Grillo, I.; Lindner, P.; Colmenero, J.; Richter, D. Equilibrium Chain Exchange Kinetics of Diblock Copolymer Micelles: Effect of Morphology. *Macromolecules* **2011**, *44* (15), 6145−6154.
(42) Lund, R.; Pipich, V.; Willner, L.; Radulescu, A.; Colmenero, J.; Richter, D. Structural and Thermodynamic Aspects of the Cylinder-to-Sphere Transition in Amphiphilic Diblock Copolymer Micelles. *Soft Matter* **2011**, *7* (4), 1491−1500.
(43) Zinn, T.; Willner, L.; Lund, R.; Pipich, V.; Richter, D. Equilibrium Exchange Kinetics in N-Alkyl-PEO Polymeric Micelles: Single Exponential Relaxation and Chain Length Dependence. *Soft Matter* **2012**, *8* (3), 623−626.
(44) Lund, R.; Willner, L.; Richter, D. Kinetics of Block Copolymer Micelles Studied by Small-Angle Scattering Methods. In *Controlled Polymerization and Polymeric Structures*; Springer International Publishing: New York, 2013; Vol. *259*, pp 51−158.
(45) Willner, L.; Poppe, A.; Allgaier, J.; Monkenbusch, M.; Richter, D. Time-Resolved SANS for the Determination of Unimer Exchange Kinetics in Block Copolymer Micelles. *Europhys. Lett.* **2001**, *55* (5), 667−673.
(46) Lund, R.; Willner, L.; Richter, D.; Dormidontova, E. E. Equilibrium Chain Exchange Kinetics of Diblock Copolymer Micelles: Tuning and Logarithmic Relaxation. *Macromolecules* **2006**, *39* (13), 4566−4575.
(47) Lund, R.; Willner, L.; Stellbrink, J.; Lindner, P.; Richter, D. Logarithmic Chain-Exchange Kinetics of Diblock Copolymer Micelles. *Phys. Rev. Lett.* **2006**, *96* (6), 1−4, DOI: 10.1103/PhysRevLett.96.068302.
(48) Fuchs, J. Ultrasonic Cleaning Fundamental Theory and Application. In *NASA. Marshall Space Flight Center, Aerospace Environmental Technology Conference*; 1995; pp 369−378.
(49) Park, R.; Choi, M.; Park, E. H.; Shon, W. J.; Kim, H. Y.; Kim, W. Comparing Cleaning Effects of Gas and Vapor Bubbles in Ultrasonic Fields. *Ultrason. Sonochem.* **2021**, *76*, No. 105618.
(50) Bu, X.; Alheshibri, M. The Effect of Ultrasound on Bulk and Surface Nanobubbles: A Review of the Current Status. *Ultrason. Sonochem.* **2021**, *76*, No. 105629.
(51) Hodge, P.; Hellwich, K. H.; Hiorns, R. C.; Jones, R. G.; Kahovec, J.; Luscombe, C. K.; Purbrick, M. D.; Wilks, E. S. *A Concise Guide to Polymer Nomenclature for Authors of Papers and Reports in Polymer Science and Technology (IUPAC Technical Report)*; 2020; Vol. *92*. DOI: 10.1515/pac-2018-0602.
(52) Prohaska, T.; Irrgeher, J.; Benefield, J.; Böhlke, J. K.; Chesson, L. A.; Coplen, T. B.; Ding, T.; Dunn, P. J. H.; Gröning, M.; Holden, N. E.; Meijer, H. A. J.; Moossen, H.; Possolo, A.; Takahashi, Y.; Vogl, J.; Walczyk, T.; Wang, J.; Wieser, M. E.; Yoneda, S.; Zhu, X. K.; Meija, J. Standard Atomic Weights of the Elements 2021 (IUPAC Technical Report). *Pure Appl. Chem.* **2022**, *94* (5), 573−600.
(53) Williams, D. B. G.; Lawton, M. Drying of Organic Solvents: Quantitative Evaluation of the Efficiency of Several Desiccants. *J. Org. Chem.* **2010**, *75* (24), 8351−8354.
(54) Heller, W. T.; Urban, V. S.; Lynn, G. W.; Weiss, K. L.; O'Neill, H. M.; Pingali, S. V.; Qian, S.; Littrell, K. C.; Melnichenko, Y. B.; Buchanan, M. V.; Selby, D. L.; Wignall, G. D.; Butler, P. D.; Myles, D. A. The Bio-SANS Instrument at the High Flux Isotope Reactor of Oak Ridge National Laboratory. *J. Appl. Crystallogr.* **2014**, *47* (4), 1238−1246.
(55) Heller, W. T.; Cuneo, M.; Debeer-Schmitt, L.; Do, C.; He, L.; Heroux, L.; Littrell, K.; Pingali, S. V.; Qian, S.; Stanley, C.; Urban, V. S.; Wu, B.; Bras, W. The Suite of Small-Angle Neutron Scattering Instruments at Oak Ridge National Laboratory. *J. Appl. Crystallogr.* **2018**, *51* (2), 242−248.
(56) Heller, W. T.; Hetrick, J.; Bilheux, J.; Calvo, J. M. B.; Chen, W.-R.; DeBeer-Schmitt, L.; Do, C.; Doucet, M.; Fitzsimmons, M. R.; Godoy, W. F.; Granroth, G. E.; Hahn, S.; He, L.; Islam, F.; Lin, J.; Littrell, K. C.; McDonnell, M.; McGaha, J.; Peterson, P. F.; Pingali, S. V.; Qian, S.; Savici, A. T.; Shang, Y.; Stanley, C. B.; Urban, V. S.; Whitfield, R. E.; Zhang, C.; Zhou, W.; Billings, J. J.; Cuneo, M. J.; Leal, R. M. F.; Wang, T.; Wu, B. Drtsans: The Data Reduction Toolkit for Small-Angle Neutron Scattering at Oak Ridge National Laboratory. *SoftwareX* **2022**, *19*, No. 101101.
(57) Browaeys, J. Linear fit with both uncertainties in x and in y; https://www.mathworks.com/matlabcentral/fileexchange/45711-linear-fit-with-both-uncertainties-in-x-and-in-y (accessed May 17, 2023).
(58) Kohlbrecher, J. User Guide for the SASfit Software Package. SASfit: A Program for Fitting Simple Structural Models to Small Angle Scattering Data. *Internet* **2019**, 688.
(59) Pedersen, J. S. Small-Angle Scattering from Surfactants and Block Copolymer Micelles. In *Soft Matter Characterization*; Borsali, R.; Pecora, R., Eds.; Springer International Publishing, 2008; pp 191−234.
(60) Pedersen, J. S.; Gerstenberg, M. C. Scattering Form Factor of Block Copolymer Micelles. *Macromolecules* **1996**, *29* (4), 1363−1365.
(61) Larison, T.; Pingali, S. V.; Stefik, M. New Approach for SANS Measurement of Micelle Chain Mixing during Size and Morphology Transitions. *Soft Matter* **2023**, *19* (19), 3487−3495.
(62) Fetters, L. J.; Lohse, D. J.; Richter, D.; Witten, T. A.; Zirkel, A. Connection between Polymer Molecular Weight, Density, Chain Dimensions, and Melt Viscoelastic Properties. *Macromolecules* **1994**, *27* (17), 4639−4647.
(63) Choi, S. H.; Bates, F. S.; Lodge, T. P. Molecular Exchange in Ordered Diblock Copolymer Micelles. *Macromolecules* **2011**, *44* (9), 3594−3604.
(64) Eskin, D. G. *Ultrasonic Degassing of Liquids*, 2nd ed.; Elsevier Ltd., 2023. DOI: 10.1016/B978-0-12-820254-8.00023-3.
(65) Eskin, G. I. Cavitation Mechanism of Ultrasonic Melt Degassing. *Ultrason. Sonochem.* **1995**, *2* (2), 137−141, DOI: 10.1016/1350-4177(95)00020-7.
(66) Richards, W. T.; Loomis, A. L. The Chemical Effects of High Frequency Sound Waves I. A Preliminary Survey. *J. Am. Chem. Soc.* **1927**, *49* (12), 3086−3100.
(67) Vencel, T.; Donovalová, J.; Gáplovský, A.; Kimura, T.; Toma, Š. Oxygen Exclusion from the Organic Solvents Using Ultrasound and Comparison with Other Common Techniques Used in Photochemical Experiments. *Chem. Pap.* **2005**, *59* (4), 271−274.

https://doi.org/10.1021/acs.macromol.3c01040
Macromolecules XXXX, XXX, XXX−XXX